Supplementary Information:

Exploring Mechanistic Routes for Light Alkane Oxidation with an Iron-Triazolate Metal–Organic Framework

Andrew S. Rosen, Justin M. Notestein,* Randall Q. Snurr*

Department of Chemical and Biological Engineering, Northwestern University, 2145 Sheridan Rd., Evanston, IL 60208 (USA)

*E-mail: j-notestein@northwestern.edu

*E-mail: snurr@northwestern.edu

Contents

Supplementary Dataset

The data accompanying this work, including input/output files, DFT-optimized structures, and tabulated energies, can be found at the Zenodo repository with the following DOI: 10.5281/zenodo.5811810.

Additional Methodological Details

Additional VASP Details

The VASP-recommended v.54 projector-augmented wave (PAW) PBE pseudopotentials[1] were used for all calculations in this work. For the HSE06-D3(BJ)//PBE-D3(BJ)+U calculations, a smaller $2 \times 1 \times 1$ k-point grid and looser SCF convergence threshold of 10^{-5} eV were used to reduce the computational cost. The PBE-D3(BJ)+U wavefunction was used as an initial guess for other levels of theory in this work. Both the atomic positions and cell volume for $Fe_2(OH)_2(\mu\text{-}OH)_2$(bbta), which was used for the Fe(III) reference in Figure 5, were fully relaxed. For calculations on Fe_2(dobdc), we used a Monkhorst-Pack[2] k-point grid of $4 \times 2 \times 2$ with the Niggli-reduced primitive cell. The settings for $Fe_2(\mu\text{-}Cl)_2$(bbta) were the same as those for $Fe_2(\mu\text{-}OH)_2$(bbta). Gas-phase species were modeled at the Γ-point only centered in a box with ~20 Å of vacuum in each dimension. As a matter of consistency, all spin density visualizations are presented at a constant isosurface value of 0.01 a.u.

Simplifying Assumptions

Due in part to the length of the reaction coordinate, the transition states associated with the radical rebound steps (particularly $\mathbf{F_2} \rightarrow \mathbf{G}$ and $\mathbf{F_3} \rightarrow \mathbf{G}$) are difficult to converge with the NEB and dimer methods although are clearly present. The methyl rebound step is often the lowest barrier in the mechanism and is occasionally neglected in prior MOF studies.[3–5] Here, we chose to calculate $\mathbf{TS_{F_1/G}}$ and used the energy of this structure for $\mathbf{TS_{F_2/G}}$ and $\mathbf{TS_{F_3/G}}$ as a first-approximation given that they all share the same final product and the transition state geometries are expected to be comparable.

Only a single barrier between $\mathbf{B_{H2O2}}$ and $\mathbf{C_{H2O}}$ was successfully isolated (i.e. for cleavage of the O–O bond in H_2O_2 but not for subsequent H-abstraction via the generated OH· radical). Given the reactive nature of the OH· species, subsequent barriers between this transient intermediate and the $\mathbf{C_{H2O}}$ products were not able to be computationally isolated, although they are likely to be small if present.

Prior theoretical calculations on the guest-free $M_2(\mu\text{-}OH)_2$(bbta) frameworks have shown that there are several low-lying configurations that the H atoms of the μ-OH^- groups can adopt, and the preferred orientation can fluctuate based on the presence of adsorbates and/or intermediates.[6,7] In this work, we generally adopted the μ-OH^- orientations used in a prior study[6] as a matter of consistency and to ensure that the relative energies were primarily associated with the catalytic transformations themselves as opposed to slight rearrangements of the μ-OH^- groups. We only changed the μ-OH^- orientation for step $\mathbf{B_{H2O2}}$ (and the subsequent transition states for H_2O_2 activation) to allow for the significantly more favorable adsorption mode of H_2O_2 (Figure S1).

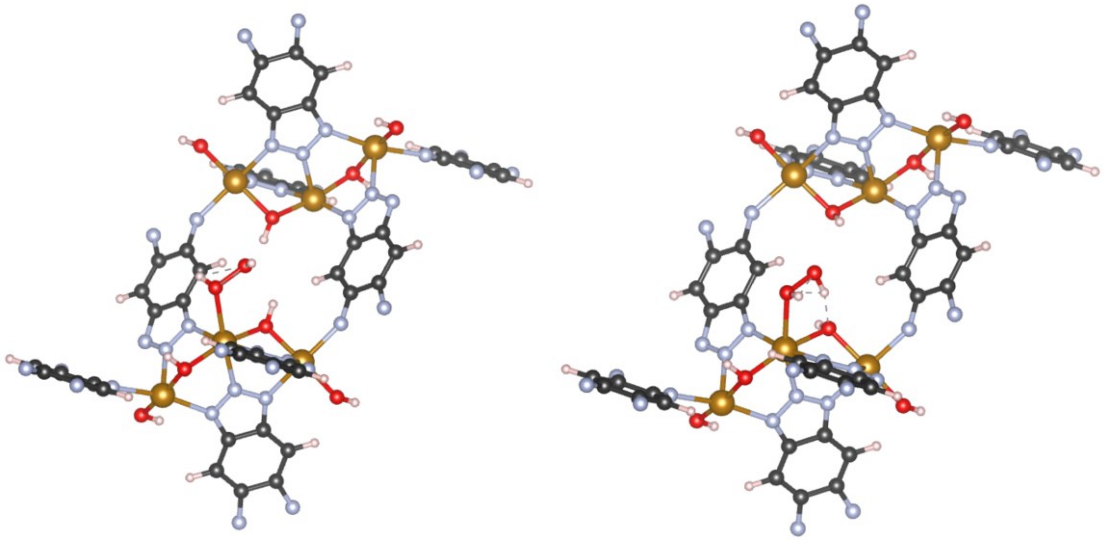

Figure S1. H_2O_2 adsorbed in two different configurations, optimized at the PBE-D3(BJ)+*U* level of theory. The structure on the right is 37 kJ/mol more stable. Color key: Fe (orange), N (blue), O (red), C (black), H (white).

In the proposed H_2O_2 mechanism, water is generated as a byproduct. We neglect the effect of water on the proposed catalytic mechanisms (except for structures $\mathbf{C_{1,H2O}}$, $\mathbf{C_{2,H2O}}$, and $\mathbf{C_{3,H2O}}$) since we primarily focus on understanding qualitative differences in electronic structure and reactivity of various active site motifs. Water adsorption in this family of metal–triazolate frameworks is known to be quite complex[8] and is beyond the scope of the present study. Nonetheless, it can be expected that certain mechanistic steps may be modified if water molecules were included throughout the H_2O_2 mechanism (e.g. the barrier for the internal H-transfer, $\mathbf{D_1} \rightarrow \mathbf{D_2}$, may be reduced if the proton could be shuttled by a nearby H_2O molecule). Additionally, H_2O molecules can potentially block the Fe(II) sites once formed. At the PBE-D3(BJ)+*U* level of theory, H_2O adsorption at a single Fe(II) site in an otherwise guest-free $Fe_2(\mu\text{-}OH)_2$(bbta) is predicted to take place with an adsorption energy of –45 kJ/mol. In practice, this might mean that the framework would need to be heated to remove bound water if the sites become saturated.

Finally, as noted in the Methods section, ferromagnetic coupling was considered between the Fe centers for computational simplicity. For reference, when using a $2 \times 1 \times 1$ supercell of the guest-free, Niggli-reduced primitive cell (which has an even number of Fe centers per chain), the antiferromagnetic (AFM) configuration with high-spin Fe sites is 1.75 kJ/mol per Fe site more stable than the analogous ferromagnetic (FM), high-spin configuration at the PBE-D3(BJ)+*U* level of theory. Here, we considered both intrachain and interchain antiferromagnetic coupling as has been done for M_2(dobdc).[9] Prior work on MIL-53(Al,Fe) has shown that the reaction profile on the AFM spin surface is comparable to that on the FM spin surface for the catalytic conversion of methane to methanol via bridging iron-oxo sites.[10] Similar observations have been reported for light alkane activation at terminal iron-oxo sites in other iron-containing MOFs as well.[4,11,12] For $Fe_2(\mu\text{-}OH)_2$(bbta), we find that for the reaction $\mathbf{A} + N_2O \rightarrow \mathbf{D_1} + N_2$, the structure with AFM coupling between Fe sites results in a reaction energy that is 3 kJ/mol more endothermic than that on the FM surface. Although this difference is quite small, we acknowledge that it is plausible that other steps in the mechanism may exhibit larger differences and would be worth investigating in future studies of this MOF family.

Structure Descriptions

The various structures considered throughout this work are described below. Refer to Scheme 1 and Scheme 2 for additional details:

- MOF with and without adsorbates:
  - **A**: Guest-free MOF
  - $\mathbf{B_{N2O}}$: **A** with an N_2O adsorbate in the η–O mode
  - $\mathbf{B_{H2O2}}$: **A** with an H_2O_2 adsorbate
  - **G**: **A** with a CH_3OH adsorbate
- $[Fe(O)]^{2+}$:
  - $\mathbf{C_{1,N2}}$: $\mathbf{B_{N2O}}$ after the activation of N_2O, resulting in an $[Fe(O)]^{2+}$ species and physisorbed N_2
  - $\mathbf{C_{1,H2O}}$: $\mathbf{B_{H2O2}}$ after the activation of H_2O_2, resulting in an $[Fe(O)]^{2+}$ species and physisorbed H_2O
  - $\mathbf{D_1}$: MOF with a single $[Fe(O)]^{2+}$ species
  - $\mathbf{E_1}$: $\mathbf{D_1}$ with a physisorbed CH_4 molecule at the terminal oxo site
  - $\mathbf{F_1}$: $\mathbf{E_1}$ after the activation of CH_4, resulting in a terminal Fe–OH species and physisorbed CH_4
- $[Fe(OH)(\mu\text{-}O)Fe]^{3+}$:
  - $\mathbf{C_{2,H2O}}$: $\mathbf{B_{H2O2}}$ after the activation of H_2O_2, resulting in an $[Fe(OH)(\mu\text{-}O)Fe]^{3+}$ species and physisorbed H_2O
  - $\mathbf{D_2}$: MOF with a single $[Fe(OH)(\mu\text{-}O)Fe]^{3+}$ species
  - $\mathbf{E_2}$: $\mathbf{D_2}$ with a physisorbed CH_4 molecule at the bridging oxo site
  - $\mathbf{F_2}$: $\mathbf{E_2}$ after the activation of CH_4, resulting in a $[Fe(OH)(\mu\text{-}OH)Fe]^{3+}$ species and physisorbed CH_4
- $[Fe(\mu\text{-}O)Fe]^{3+}$:
  - $\mathbf{C_{3,H2O}}$: $\mathbf{B_{H2O2}}$ after the activation of H_2O_2, resulting in an $[Fe(\mu\text{-}O)Fe]^{3+}$ species (and Fe–OH species on the opposite chain of iron sites) and physisorbed H_2O
  - $\mathbf{D_3}$: MOF with a single $[Fe(\mu\text{-}O)Fe]^{3+}$ species (and Fe–OH species on the opposite chain of iron sites) per cell
  - $\mathbf{E_3}$: $\mathbf{D_3}$ with a physisorbed CH_4 molecule at the bridging oxo site
  - $\mathbf{F_3}$: $\mathbf{E_3}$ after the activation of CH_4, resulting in a $[Fe(\mu\text{-}OH)Fe]^{3+}$ species and physisorbed CH_4
- $[Fe(OH)(\mu\text{-}O)Fe(OH)]^{3+}$ (not shown in Scheme 1 or Scheme 2 but discussed in Figure 5 and Tables S9 and S13):
  - $\mathbf{D_4}$: MOF with a single $[Fe(OH)(\mu\text{-}O)Fe(OH)]^{3+}$ species
  - $\mathbf{E_4}$: $\mathbf{D_4}$ with a physisorbed CH_4 molecule at the bridging oxo site
  - $\mathbf{F_4}$: $\mathbf{E_4}$ after the activation of CH_4, resulting in a $[Fe(OH)(\mu\text{-}OH)Fe(OH)]^{3+}$ species and physisorbed CH_4

DFT-Optimized Lattice Constants

The DFT-optimized lattice constants for the guest-free $Fe_2(\mu\text{-}OH)_2(bbta)$ and $Fe_2(\mu\text{-}Cl)_2(bbta)$ structures are shown in Table S1 and Table S2, respectively. Excellent agreement between theory and experiment is observed for the previously synthesized $Fe_2(\mu\text{-}Cl)_2(bbta)$ structure (Table S2).

Table S1. Computed lattice constants for $Fe_2(\mu\text{-}OH)_2(bbta)$ at the PBE-D3(BJ)+U level of theory.

MOF	a (Å)	b (Å)	c (Å)	α (°)	β (°)	γ (°)

$Fe_2(\mu\text{-}OH)_2(bbta)$	8.12	15.07	15.10	116.3	101.0	100.0

Table S2. Computed ("Theory") and experimentally derived ("Exp.") lattice constants for $Fe_2(\mu\text{-}Cl)_2(bbta)$ at the PBE-D3(BJ)+U level of theory.

MOF		a (Å)	b (Å)	c (Å)	α (°)	β (°)	γ (°)
$Fe_2(\mu\text{-}Cl)_2(bbta)$	Theory	8.28	14.88	14.88	116.6	100.7	100.7
	Exp.[13]	8.23	14.78	14.78	116.6	100.7	100.7

Spin States for $Fe_2(\mu\text{-}OH)_2(bbta)$

The spin states considered throughout this work are shown in Table S3 based on an energetic comparison of various plausible spin states at the PBE-D3(BJ)+U level of theory. Generally, the iron species tend to exist in the high-spin configuration. For a detailed description of the individual magnetic moments, refer to the supporting dataset.

Table S3. Spin states of each structure considered in this work where S is the total spin quantum number (per unit cell). Note that there are a total of six Fe cations in the $Fe_2(\mu\text{-}OH)_2(bbta)$ unit cell, such that a value of $2S = 24$ as in structure **A** would imply that there are four unpaired electrons per iron center.

Structure	$2S$
A	24
$\mathbf{B_{N2O}}$	24
$\mathbf{B_{H2O2}}$	24
$\mathbf{C_{1,N2}}$	24
$\mathbf{C_{1,H2O}}$	24
$\mathbf{C_{2,H2O}}$	26
$\mathbf{C_{3,H2O}}$	26
$\mathbf{D_1}$	24
$\mathbf{D_2}$	26
$\mathbf{D_3}$	26
$\mathbf{D_4}$	27
$\mathbf{E_1}$	24
$\mathbf{E_2}$	26
$\mathbf{E_3}$	26
$\mathbf{E_4}$	27
$\mathbf{F_1}$	24
$\mathbf{F_2}$	24
$\mathbf{F_3}$	24
$\mathbf{F_4}$	25
G	24
$\mathbf{TS_{B_{N2O}/C_{1,N2O}}}$	24
$\mathbf{TS_{B_{H2O2}/C_{1,H2O}}}$	24
$\mathbf{TS_{B_{H2O2}/C_{2,H2O}}}$	24
$\mathbf{TS_{B_{H2O2}/C_{3,H2O}}}$	24
$\mathbf{TS_{D_1/D_2}}$	24
$\mathbf{TS_{E_1/F_1}}$	24
$\mathbf{TS_{E_2/F_2}}$	24
$\mathbf{TS_{E_3/F_3}}$	24

$\mathbf{TS_{E_4/F_4}}$	25
$\mathbf{TS_{F/G}}$	24

Supplementary Results

Tabulated Energies and Geometries

Two N_2O adsorption modes at the Fe sites of $Fe_2(\mu\text{-}OH)_2(bbta)$ are shown in Figure S2 with their corresponding adsorption energies in Table S4.

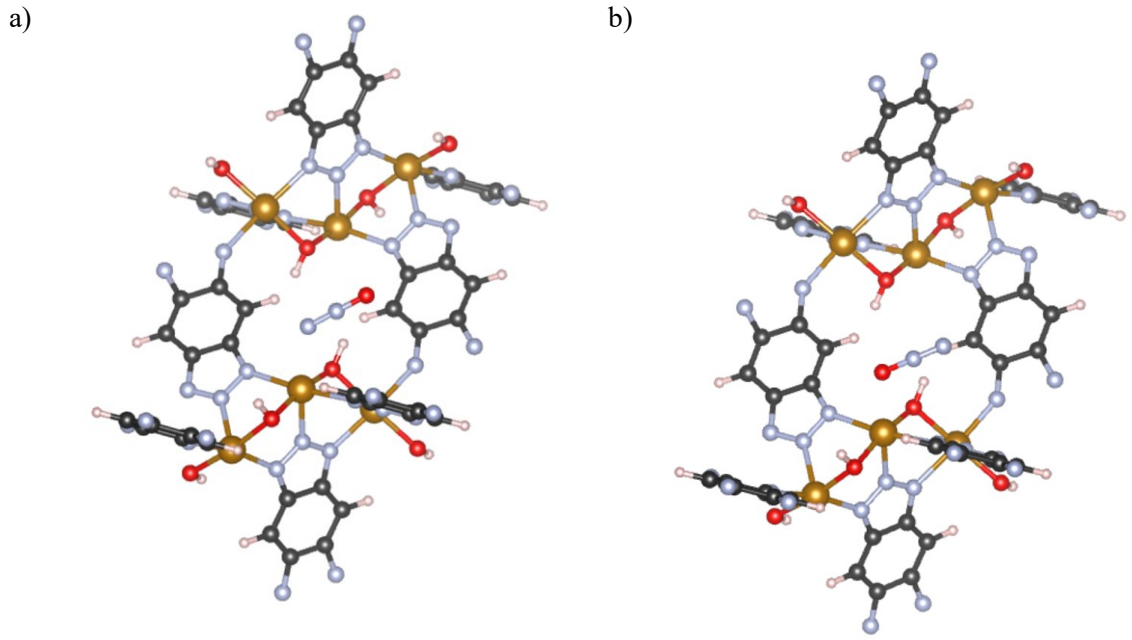

Figure S2. a) N_2O adsorbed in an η^1–N mode at the Fe center of $Fe_2(\mu\text{-}OH)_2(bbta)$. b) N_2O adsorbed in an η^1–O mode at the Fe center of $Fe_2(\mu\text{-}OH)_2(bbta)$. The structures shown are DFT-optimized at the PBE-D3(BJ)+U level of theory. Color key: Fe (orange), N (blue), O (red), C (black), H (white).

Table S4. N_2O adsorption energies ($\mathbf{A} + N_2O \rightarrow \mathbf{B_{N2O}}$) for $Fe_2(\mu\text{-}OH)_2(bbta)$ at the PBE-D3(BJ)+U level of theory.

Adsorption mode	ΔE (kJ/mol)
η^1–N	–24
η^1–O	–22

Table S5. Key geometric parameters, including the Fe–O distance, N–O distance, Fe–O–N angle, and N–O–O bond angle at the transition state for N_2O activation ($\mathbf{TS_{B_{N2O}/C_{1,N2}}}$) at the PBE-D3(BJ)+$U$ level of theory. For reference, the N–O distance and N–O–O angle in free N_2O are 1.20 Å and 180.0° at the same level of theory.

MOF	d_{Fe-O} (Å)	d_{N-O} (Å)	$\angle_{Fe-O-N}$ (°)	$\angle_{N-O-O}$ (°)
$Fe_2(\mu\text{-}OH)_2(bbta)$	1.88	1.53	129	133
$Fe_2(dobdc)$	1.84	1.55	134	135

Table S6. N_2O activation energies ($\mathbf{B_{N2O}} \rightarrow \mathbf{TS_{B_{N2O}/C_{1,N2}}}$) at the PBE-D3(BJ)+$U$ level of theory.*

MOF	$E_{a,N_2O\ act.}$ (kJ/mol)
$Fe_2(\mu\text{-}OH)_2(bbta)$	102
$Fe_2(dobdc)$	129
$Fe_2(\mu\text{-}Cl)_2(bbta)$	143

*Prior work on $Fe_{0.1}Mg_{1.9}(dobdc)$ predicts $E_{a,N2O\ act.}$ to be 97 kJ/mol at the M06-L level of theory.[14] As discussed in greater detail below (e.g. Table S12), the N_2O activation energy is highly sensitive to the level of theory, specifically whether or not it includes Hartree-Fock exchange or a $+U$ correction.

Table S7. Reaction energy associated with metal-oxo formation ($\mathbf{B_{N2O}} \rightarrow \mathbf{C_{1,N2}}$) at the PBE-D3(BJ)+$U$ level of theory.*

MOF	ΔE (kJ/mol)
$Fe_2(\mu\text{-}OH)_2(bbta)$	–15
$Fe_2(dobdc)$	17

*Prior work on $Fe_{0.1}Mg_{1.9}(dobdc)$ predicts ΔE to be –70 kJ/mol at the M06-L level of theory.[14] As discussed in greater detail below (e.g. Table S10), the metal-oxo formation energy is highly sensitive to the level of theory, specifically whether or not it includes Hartree-Fock exchange or a $+U$ correction.

Table S8. C–H activation barriers at the terminal metal-oxo species ($\mathbf{E_1} \rightarrow \mathbf{TS_{E_1/F_1}}$) at the PBE-D3(BJ)+$U$ level of theory.*

MOF	$E_{a,C-H\ act.}$ (kJ/mol)
$Fe_2(dobdc)$	44
$Fe_2(\mu\text{-}OH)_2(bbta)$	67

*At the B3LYP/6-31G** level of theory with dispersion corrections, the barrier is predicted to be 51 kJ/mol for $Fe_2(dobdc)$.[15]

$\mathbf{TS_{B_{N2O}/C_1}}$

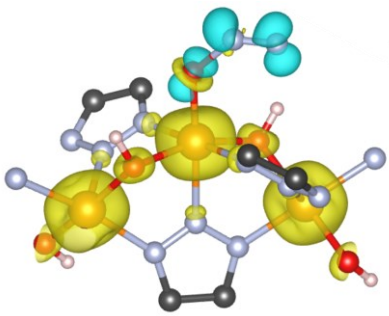

$\mathbf{TS_{B_{H2O2}/C_1}}$

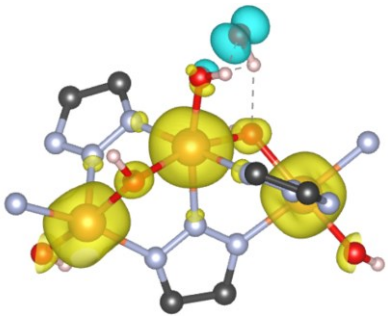

$\mathbf{TS_{B_{H2O2}/C_2}}$

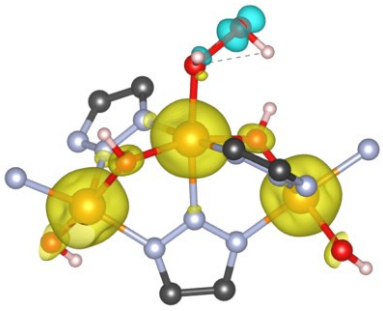

$\mathbf{TS_{B_{H2O2}/C_3}}$

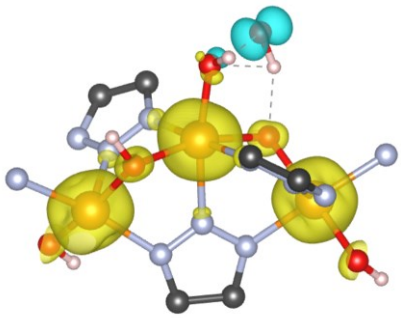

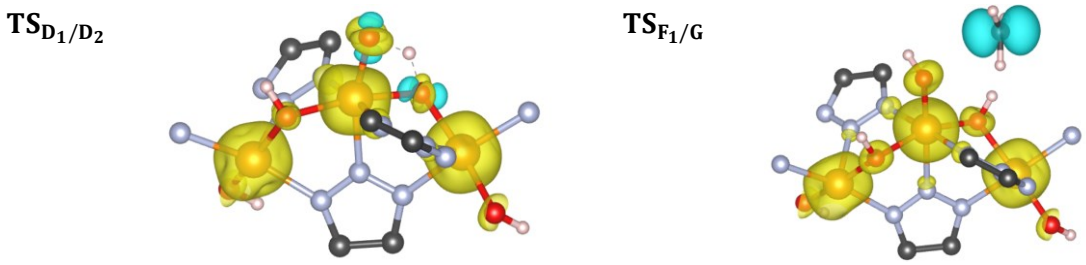

Figure S3. Spin densities for several transition states considered in this work at the PBE-D3(BJ)+*U* level of theory. Note that the spin density on the peripheral oxygen atoms is truncated due to periodic boundary conditions and that the viewing angles are slightly different for ease-of-visualization. Spin density color key: positive spin density (yellow), negative spin density (cyan). Atom color key: Fe (orange), O (red), N (blue), C (black), H (white).

Additional Results at the PBE-D3(BJ)+*U* Level of Theory

The mechanistic pathway for methane to methanol conversion in the presence of N_2O (including internal H-transfer to go from $\mathbf{D_1}$ to $\mathbf{D_2}$) is shown in Figure S4.

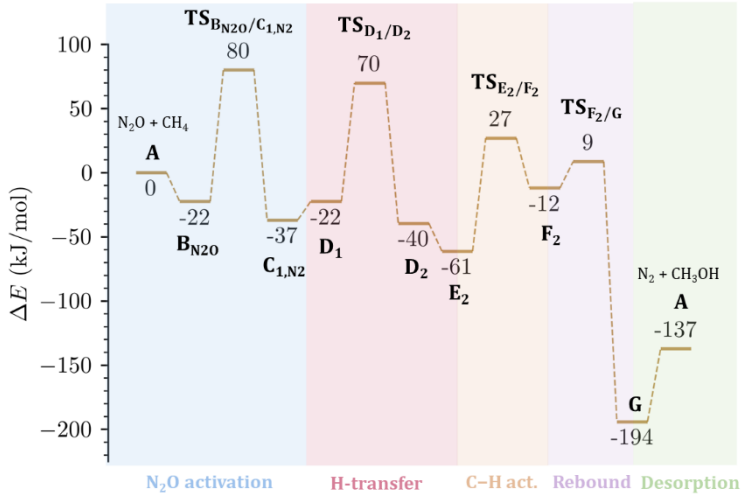

Figure S4. Potential energy landscape for the conversion of methane to methanol via a bridging iron-oxo species formed in the presence of an N_2O oxidant and an $Fe_2(\mu\text{-}OH)_2$(bbta) catalyst following an internal H-transfer mechanism. The zero-energy reference corresponds to the infinitely separated reactants (i.e. **A** + N_2O + CH_4). Results are presented at the PBE-D3(BJ)+*U* level of theory.

The transition state for the surface-stabilized (i.e. concerted) methane dissociation route at the $\mathbf{D_2}$ active site is shown in Figure S5. The kinetic barrier for the C–H activation process is 103 kJ/mol at the PBE-D3(BJ)+*U* level of theory.

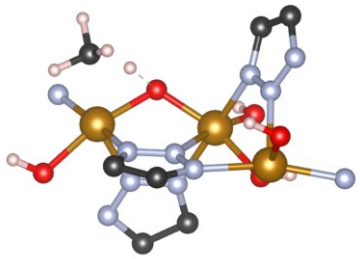

Figure S5. Transition state structure for surface-stabilized methane dissociation at the $\mathbf{D_2}$ site at the PBE-D3(BJ)+*U* level of theory. Color key: Fe (orange), N (blue), O (red), C (black), H (white).

Understanding the Impact of +*U*

To better understand the role of the +*U* correction, we have isolated several of the intermediates and transition states at the PBE-D3(BJ) (i.e. $U = 0$ eV) level of theory.

Beginning with a Bader analysis, we find that the inclusion of a +*U* correction tends to increase the spin density on the metal centers while decreasing the spin density on the terminal/bridging oxo ligands (Table S9). The greater delocalization of the spin density from the metal centers to the surrounding ligands with PBE can likely be traced back to the self-interaction error. Analogous spin density trends were observed in prior work on Fe_2(dobdc) when comparing PBE results against those at the B3LYP level of theory,[16] suggesting that the +*U* correction is mimicking the behavior of the hybrid functional in this regard.

Table S9. Bader spin densities ρ for different iron-oxo species in $Fe_2(\mu\text{-}OH)_2$(bbta) at the PBE-D3(BJ) and PBE-D3(BJ)+*U* levels of theory. Metals 1 and 2 refer to the atoms surrounding the bridging oxygen species, except for $\mathbf{D_1}$ where only the metal of the terminal metal-oxo species is considered.

Structure	PBE-D3(BJ)			PBE-D3(BJ)+*U*		
	$\lvert\rho_{Fe_1}\rvert$	$\lvert\rho_{Fe_2}\rvert$	$\lvert\rho_O\rvert$	$\lvert\rho_{Fe_1}\rvert$	$\lvert\rho_{Fe_2}\rvert$	$\lvert\rho_O\rvert$
$\mathbf{D_1}$	2.92	—	0.60	3.36	—	0.43
$\mathbf{D_2}$	4.00	3.83	0.69	4.23	4.15	0.63
$\mathbf{D_3}$	3.95	3.78	0.66	4.13	3.75	0.60
$\mathbf{D_4}$	4.00	4.00	0.70	4.19	4.19	0.58

We also find that the +*U* correction makes the iron-oxo formation energies less exothermic compared to $U = 0$ eV in all cases (Tables S10 and S11). This is to be expected and is consistent with prior work showing that the coordinatively unsaturated metal centers of transition metal complexes[17] and MOFs[18] are predicted to be too easily oxidized with generalized gradient approximation (GGA) functionals. The iron-oxo formation energies are drastically different depending on whether a +*U* correction is applied or not, and the relative stabilities of different metal-oxo motifs are not necessarily the same (Table S11). Similarly, the barriers for N_2O activation and H_2O_2 activation are higher with the +*U* correction than without (Table S12).

Table S10. Comparison of the metal-oxo formation energy (in the presence of N_2O) at the PBE-D3(BJ) and PBE-D3(BJ)+*U* levels of theory with $Fe_2(\mu\text{-}OH)_2$(bbta).

Theory	$\Delta E_{\mathbf{B_{N2O}\rightarrow C_{1,N2}}}$ (kJ/mol)
PBE-D3(BJ)	–147
PBE-D3(BJ)+*U*	–15

Table S11. Comparison of the metal-oxo formation energies (in the presence of H_2O_2) at the PBE-D3(BJ) and PBE-D3(BJ)+*U* levels of theory with $Fe_2(\mu\text{-}OH)_2$(bbta).

Theory	$\Delta E_{\mathbf{B_{H2O2}\rightarrow D_1}}$ (kJ/mol)	$\Delta E_{\mathbf{B_{H2O2}\rightarrow D_2}}$ (kJ/mol)	$\Delta E_{\mathbf{B_{H2O2}\rightarrow D_3}}$ (kJ/mol)
PBE-D3(BJ)	–154	–131	–147
PBE-D3(BJ)+*U*	–21	–38	–35

Table S12. Comparison of the N_2O and H_2O_2 activation barriers at the PBE-D3(BJ) and PBE-D3(BJ)+*U* levels of theory with $Fe_2(\mu\text{-}OH)_2$(bbta).

Theory	$\mathbf{B_{N2O} \rightarrow TS_{B_{N2O}/C_{1,N2}}}$ (kJ/mol)	$\mathbf{B_{H2O2} \rightarrow TS_{B_{H2O2}/C_{1,H2O}}}$ (kJ/mol)
PBE-D3(BJ)	53	19
PBE-D3(BJ)+*U*	102	51

The barriers for methane activation at the PBE-D3(BJ)+*U* level of theory tend to be smaller than those without a +*U* correction (Table S13). This finding is also consistent with prior studies. For instance, it was previously shown that the activation energy for cleaving the C–H bond of ethane at $[Fe(O)]^{2+}$ sites of Fe_2(dobdc) is 29 kJ/mol, 65 kJ/mol, and 101 kJ/mol with the M06 (meta-hybrid GGA), B3LYP (hybrid GGA), and BP86 (GGA) functionals, respectively.[19] These barriers are inversely correlated with the fraction of Hartree-Fock (HF) exchange of each functional (27%, 20%, and 0%, respectively), suggesting that the barrier for C–H activation may be too high with common GGA functionals and can be lowered by including HF exchange. Therefore, it is reassuring that the +*U* correction addresses this presumed limitation of PBE, although the optimal values for *U* will inevitably differ from the values employed in the present work. The lower C–H activation barriers when the +*U* correction is employed can likely be traced back, at least in part, to the less stable iron-oxo species, which in turns reduces the barrier for C–H activation.[20]

Table S13. Comparison of the methane activation barriers at the PBE-D3(BJ) and PBE-D3(BJ)+*U* levels of theory.

Theory	$\mathbf{E_1 \rightarrow TS_{E_1/F_1}}$ (kJ/mol)	$\mathbf{E_2 \rightarrow TS_{E_2/F_2}}$ (kJ/mol)	$\mathbf{E_3 \rightarrow TS_{E_3/F_3}}$ (kJ/mol)	$\mathbf{E_4 \rightarrow TS_{E_4/F_4}}$ (kJ/mol)
PBE-D3(BJ)	139	116	128	106
PBE-D3(BJ)+*U*	67	88	82	68

Additional Results at the HSE06-D3(BJ)//PBE-D3(BJ)+*U* Level of Theory

Currently, the gold-standard for solid-state DFT calculations is the HSE06 screened-hybrid functional.[21,22] However, full structure relaxations using the HSE06 functional were found to be prohibitively expensive for the materials studied in the present work. Nonetheless, to explore the possible effects of a functional with HF exchange, we ran static HSE06-D3(BJ) calculations on the PBE-D3(BJ)+*U* geometries, denoted HSE06-D3(BJ)//PBE-D3(BJ)+*U*. These results are shown in Figures S6–S8.

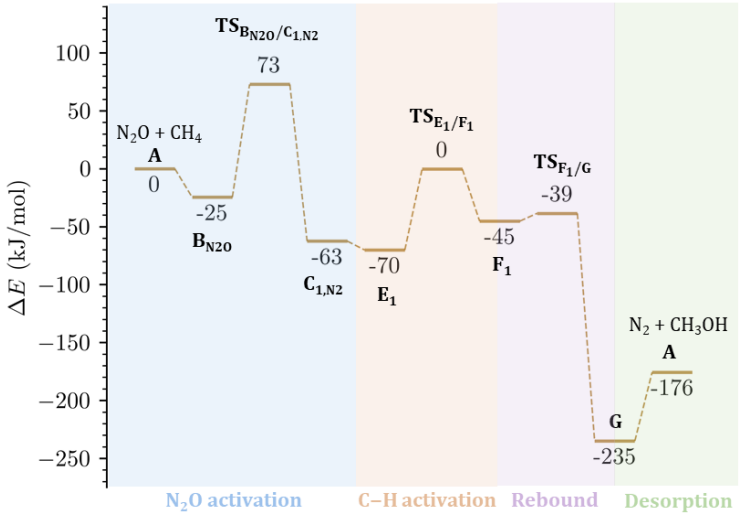

Figure S6. Potential energy landscape for the conversion of methane to methanol via a terminal iron-oxo species formed in the presence of an N_2O oxidant and an $Fe_2(\mu\text{-}OH)_2$(bbta) catalyst. The zero-energy reference corresponds to the infinitely separated reactants (i.e. **A** + N_2O + CH_4). Results are presented at the HSE06-D3(BJ)//PBE-D3(BJ)+*U* level of theory.

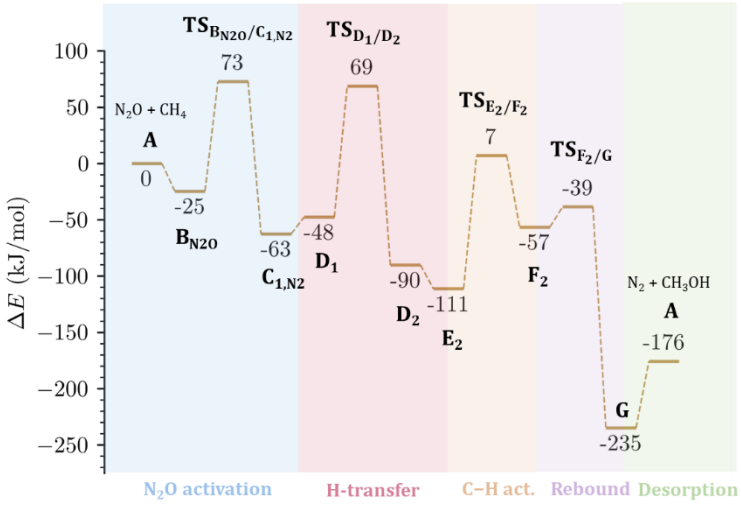

Figure S7. Potential energy landscape for the conversion of methane to methanol via a bridging iron-oxo species formed in the presence of an N_2O oxidant and an $Fe_2(\mu\text{-}OH)_2$(bbta) catalyst following an internal H-transfer mechanism. The zero-energy reference corresponds to the infinitely separated reactants (i.e. **A** + N_2O + CH_4). Results are presented at the HSE06-D3(BJ)//PBE-D3(BJ)+*U* level of theory.

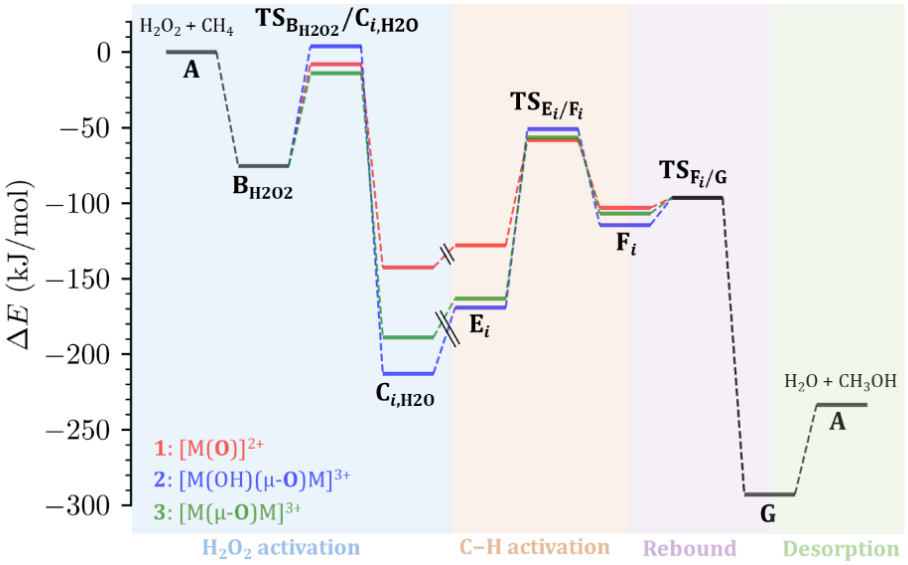

Figure S8. Potential energy landscape for the conversion of methane to methanol in the presence of an H_2O_2 oxidant and $Fe_2(\mu\text{-}OH)_2(bbta)$ catalyst. The zero-energy reference corresponds to the infinitely separated reactants (**A** + H_2O_2 + CH_4). Results are presented at the HSE06-D3(BJ)//PBE-D3(BJ)+*U* level of theory. Color key: $[Fe(O)]^{2+}$ (red), $[Fe(OH)(\mu\text{-}O)Fe]^{3+}$ (blue), and $[Fe(\mu\text{-}O)Fe]^{3+}$ (green) pathways.

Supplementary References

(1) Blöchl, P. E. Projector Augmented-Wave Method. *Phys. Rev. B* **1994**, *50* (24), 17953–17979.

(2) Monkhorst, H. J.; Pack, J. D. Special Points for Brillouin-Zone Integrations. *Phys. Rev. B* **1976**, *13* (12), 5188–5192.

(3) Barona, M.; Ahn, S.; Morris, W.; Hoover, W. J.; Notestein, J. M.; Farha, O. K.; Snurr, R. Q. Computational Predictions and Experimental Validation of Alkane Oxidative Dehydrogenation by Fe_2M MOF Nodes. *ACS Catal.* **2020**, *10* (2), 1460–1469.

(4) Barona, M.; Snurr, R. Q. Exploring the Tunability of Trimetallic MOF Nodes for Partial Oxidation of Methane to Methanol. *ACS Appl. Mater. Interfaces* **2020**, *12* (25), 28217–28231.

(5) Vitillo, J. G.; Lu, C. C.; Cramer, C. J.; Bhan, A.; Gagliardi, L. Influence of First and Second Coordination Environment on Structural Fe(II) Sites in MIL-101 for C–H Bond Activation in Methane. *ACS Catal.* **2020**, *11*, 579–589.

(6) Rosen, A. S.; Mian, M. R.; Islamoglu, T.; Chen, H.; Farha, O. K.; Notestein, J. M.; Snurr, R. Q. Tuning the Redox Activity of Metal−Organic Frameworks for Enhanced, Selective O_2 Binding: Design Rules and Ambient Temperature O_2 Chemisorption in a Cobalt−Triazolate Framework. *J. Am. Chem. Soc.* **2020**, *142* (9), 4317–4328.

(7) Oktawiec, J.; Jiang, H. Z. H.; Vitillo, J. G.; Reed, D. A.; Darago, L. E.; Trump, B. A.; Bernales, V.; Li, H.; Colwell, K. A.; Furukawa, H.; Brown, C. M.; Gagliardi, L.; Long, J. R. Negative Cooperativity upon Hydrogen Bond-Stabilized O_2 Adsorption in a Redox-Active Metal–Organic Framework. *Nat. Commun.* **2020**, *11*, 3087.

(8) Rieth, A. J.; Hunter, K. M.; Dincă, M.; Paesani, F. Hydrogen Bonding Structure of Confined Water Templated by a Metal-Organic Framework with Open Metal Sites. *Nat. Commun.* **2019**, *10*, 4771.

(9) Zhang, Q.; Li, B.; Chen, L. First-Principles Study of Microporous Magnets M-MOF-74 (M= Ni, Co, Fe, Mn): The Role of Metal Centers. *Inorg. Chem.* **2013**, *52* (16), 9356–9362.

(10) Szécsényi, Á.; Li, G.; Gascon, J.; Pidko, E. A. Unraveling Reaction Networks behind the Catalytic Oxidation of Methane with H_2O_2 over a Mixed-Metal MIL-53(Al,Fe) MOF Catalyst. *Chem. Sci.* **2018**, *9* (33), 6765–6773.

(11) Simons, M. C.; Vitillo, J. G.; Babucci, M.; Hoffman, A. S.; Boubnov, A.; Beauvais, M. L.; Chen, Z.; Cramer, C. J.; Chapman, K. W.; Bare, S. R.; Gates, B. C.; Lu, C. C.; Gagliardi, L.; Bhan, A. Structure, Dynamics, and Reactivity for Light Alkane Oxidation of Fe(II) Sites Situated in the Nodes of a Metal–Organic Framework. *J. Am. Chem. Soc.* **2019**, *141* (45), 18142–18151.

(12) Vitillo, J. G.; Bhan, A.; Cramer, C. J.; Lu, C. C.; Gagliardi, L. Quantum Chemical Characterization of Structural Single Fe(II) Sites in MIL-Type Metal Organic Frameworks for Oxidation of Methane to Methanol and Ethane to Ethanol. *ACS Catal.* **2019**, *9*, 2870–2879.

(13) Reed, D. A.; Keitz, B. K.; Oktawiec, J.; Mason, J. A.; Runčevski, T.; Xiao, D. J.; Darago, L. E.; Crocellà, V.; Bordiga, S.; Long, J. R. A Spin Transition Mechanism for Cooperative Adsorption in Metal−Organic Frameworks. *Nature* **2017**, *550* (7674), 96–100.

(14) Verma, P.; Vogiatzis, K. D.; Planas, N.; Borycz, J.; Xiao, D. J.; Long, J. R.; Gagliardi, L.; Truhlar, D. G. Mechanism of Oxidation of Ethane to Ethanol at Iron(IV)-Oxo Sites in Magnesium-Diluted Fe_2(DOBDC). *J. Am. Chem. Soc.* **2015**, *137* (17), 5770–5781.

(15) Saiz, F.; Bernasconi, L. Electronic Structure and Reactivity of Fe(IV) Oxo Species in Metal--Organic Frameworks. *Phys. Chem. Chem. Phys.* **2019**, *21* (9), 4965–4974.

(16) Saiz, F.; Bernasconi, L. Density-Functional Theory Models of Fe(IV)O Reactivity in Metal–Organic Frameworks: Self-Interaction Error, Spin Delocalisation and the Role of Hybrid Exchange. *Phys. Chem. Chem. Phys.* **2020**, *22* (22), 12821–12830.

(17) Vennelakanti, V.; Nandy, A.; Kulik, H. The Effect of Hartree-Fock Exchange on Scaling Relations and Reaction Energetics for C--H Activation Catalysts. *Top. Catal.* **2021**.

(18) Rosen, A. S.; Notestein, J. M.; Snurr, R. Q. Comparing GGA, GGA+U, and Meta-GGA Functionals for Redox-Dependent Binding at Open Metal Sites in Metal−Organic Frameworks. *J. Chem. Phys.* **2020**, *152*, 224101.

(19) Hirao, H.; Ng, W. K. H.; Moeljadi, A. M. P.; Bureekaew, S. Multiscale Model for a Metal−Organic Framework: High-Spin Rebound Mechanism in the Reaction of the Oxoiron(IV) Species of Fe-MOF-74. *ACS Catal.* **2015**, *5* (6), 3287–3291.

(20) Rosen, A. S.; Notestein, J. M.; Snurr, R. Q. Structure−Activity Relationships That Identify Metal−Organic Framework Catalysts for Methane Activation. *ACS Catal.* **2019**, *9*, 3576–3587.

(21) Heyd, J.; Scuseria, G. E.; Ernzerhof, M. Hybrid Functionals Based on a Screened Coulomb Potential. *J. Chem. Phys.* **2003**, *118* (18), 8207–8215.

(22) Krukau, A. V; Vydrov, O. A.; Izmaylov, A. F.; Scuseria, G. E. Influence of the Exchange Screening Parameter on the Performance of Screened Hybrid Functionals. *J. Chem. Phys.* **2006**, *125* (22), 224106.